Molecular dynamics study of melting of the HCP metal Mg

P. Bavli, E. Polturak, and Joan Adler*
Physics Department, Technion-Israel Institute of Technology, Haifa 32000, Israel
(Dated: September 12, 2011)

We present molecular dynamics simulations of the melting transition of Mg, an HCP metal, using the potential developed by Sun et al. This study was motivated by the question of whether the hierarchy of premelting phenomena, found to occur between different facets of metals with an FCC or BCC structure, is also present in HCP metals. We first determined the structural and energetic properties of the effectively infinite solid with no boundaries. We then investigated the low-index surfaces of Mg, namely the **c** (0001), **a** ($10\overline{1}0$) and **s** ($10\overline{1}1$) facets. We found that as the temperature increases, the ($10\overline{1}0$) surface disorders first, followed by the ($10\overline{1}1$) surface, while the (0001) surface remains stable up to the melting temperature. The disorder spreads from the surface into the bulk, establishing a thin quasiliquid film in the surface region. We conclude that the effect of premelting phenomena is inversely proportional to the surface atomic density, being most pronounced at the **a** ($10\overline{1}0$) facet which has the lowest density. This conclusion is in line with the behavior found for FCC and BCC metals.

PACS numbers: 42.87.-d, 74.25.Qt

I. INTRODUCTION

Theories of melting[1–3] can be separated into two classes. The first one describes the mechanical melting of a homogeneous solid resulting from lattice instability[4–6] and/or the spontaneous[7–11] generation of thermal defects. The second class treats the thermodynamic melting of heterogeneous solids, which begins at extrinsic defects such as a free surface or an internal interface grain boundary, void, etc.[12–17] Theoretical aspects of melting beginning at the surface have been studied by phenomenological theories[13,20–22], lattice-gas models[14], and density functional theory[23]. Microscopic descriptions of static and dynamic properties of melting phenomena beginning at a surface emerged from computer simulations which employ many-body interaction potentials derived from the effective-medium[24–26] and embedded-atom theories,[15–17,27–29] as well as pairwise interatomic interactions in the form of Lennard-Jones potentials.[30,31]

Experiments[12,13] show that melting at the surface is anisotropic, meaning that certain surfaces of fcc metals such as Pb(110), Al(110) exhibit premelting, while the close-packed surfaces such as Pb(111), Al(111) do not. Theoretical aspects of this anisotropy were discussed by Trayanov and Tosatti[14] within a mean-field approximation.

Over several years, we have systematically explored the issue of whether any of the attributes of melting are different for solids having different lattice symmetry. We use molecular dynamics (MD) simulations, which is a a natural approach to treat a dynamic process such as melting. We began our program[11] with the FCC metal Cu, that has also been studied by others[10,32–34]. We continued our program[18,19] with a BCC metal V. At first[11] we were concerned with melting in the bulk and the role of points defects in this process. In the next stage[19], we also began to simulate melting on surfaces. In our investigation of the low-index surfaces of BCC vanadium, V(111), V(001), and V(011), we found results similar to those from experiment and mean-field theory mentioned above. Specifically, we observed that as the temperature increases, the V(111) surface disorders first, then the V(100) surface, while the V(110) surface remains stable up to the melting temperature, T_m. It appears that the order at which premelting phenomena appear is inversely proportional to the surface atomic density, being most pronounced for the surface which has the lowest density.

The present simulations are an extension of these studies to a non-Bravais HCP metal, Mg. (The earlier simulations of ours and others mentioned above were all made for cubic Bravais lattices.) The more complex HCP lattice has an interesting facet structure. We have studied the mechanical melting transition of the bulk HCP solid without surfaces as well as the thermodynamic melting of the solid with a free surface. The samples with an exposed, free surface were constructed so that the free surface takes one of the 3 different orientations **c**, **a** and **s**. These main facets of the equilibrium crystal shape with nearest neighbour interactions at T=0, are shown[35] in Figure 1. Our aim in this study is to search for a similar hierarchy of premelting phenomena among the surfaces of the HCP metal.

This paper is organized as follows: technical details about the lattice and our molecular dynamics simulations are presented in Section II. Section III deals with mechanical melting of a bulk Mg crystal with no free surface, and provides validation of the algoritm, code and analysis tools. Sec IV contains most of the results of this study, including the thermodynamic melting temperature and several structural and energetic properties of the various surfaces. In Section V we summarize and discuss the implications of this study.

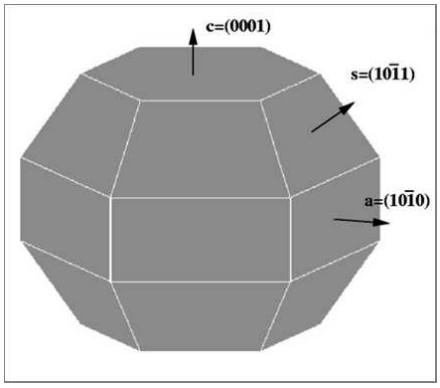

FIG. 1: Equilibrium shape of the HCP crystal at T=0 showing the locations of the main facets, and their Miller indices[35].

II. SIMULATION DETAILS

Magnesium is a metal with a nearly ideal HCP structure. The HCP structure is not Bravais, but is constructed from two simple hexagonal Bravais lattices. During our discussion of bulk melting, we call the plane where they have a triangular structure, the XY plane,(using upper case letters) with a nearest neighbour lattice spacing of a. The XY planes are displaced in the perpendicular, Z, direction by a distance of $c/2$. The equilibrium shape[35] of an HCP crystal at T=0 is shown in Figure 1. We will redefine the axes when we describe the surface melting and use the lower case variables x, y and z which will change directions as appropriate for each facet.

A. Integrators and potentials

A new MD code was written for this project, because the structure of the surface facets is so complex. Although the initial and boundary conditions of the simulations differ for the bulk and surface cases many issues are common to both situations. We have integrated the equations of motion with the predictor-corrector method[36,37] which is appropriate here because we need to determine the positions of atoms with good accuracy to avoid unphysical instabilities.

Since magnesium is a metal, simple pair-wise potentials of the Lennard Jones family are inadequate as they enforce the Cauchy relation that should not be valid for metals. The Embedded Atom (EAM) family, which has an additional many-body interaction is better suited. We selected an EAM potential for magnesium that was developed by Sun et al.[38] The potential was developed by fitting to both experimentally measured properties and to others calculated from first principles. These include properties of both crystalline and liquid bulk phases, including the melting temperatures T_m for HCP and metastable BCC solids. The potential is an extension of earlier study by Liu et al.[39] who developed an EAM potential for Mg by employing the force-matching method. The advance of Sun et al. relative to Liu et al, is that Liu's potential gives rise to an HCP-BCC transition upon heating at zero pressure, such that the coexistence between HCP Mg and the liquid phase at the HCP melting point is metastable. Such metastability can potentially lead to artifacts in simulating melt coexistence and crystallization kinetics. In Sun's potential this problem was corrected and it gives rise to stable coexistence between the HCP crystal and its melt. Another desirable feature of the potential is that, due to the use of the melting temperature in its fitting, the potential yields melting properties for HCP Mg in very reasonable agreement with experimental measurements[40].

Determination of T_m and additional properties such as thermal expansion for the bulk served to validate our code and show that it gives consistent results, as will be shown below. Once this was established, we could continue onwards to our primary aim of observing melting on different facets.

B. Ensembles

The potential described above defines the behavior of the system while it is held at constant pressure and/or temperature. Although there are advantages of simulations over experiments when it comes to viewing or recording atomic positions, issues related to conservation or otherwise of volume, temperature etc, can be complex in simulation. In addition to simulations in the NVE ensemble which conserves energy, E, number of particles, N and volume, V, we used the NVT ensemble extensively where instead of energy conservation the temperature T is kept constant. The temperature of a system is defined through the kinetic energy of the particles. Several methods have been developed to control temperature in molecular dynamics simulations. These include differential, proportional, stochastic and the integral thermostat[41], also known as the extended system method or the Nose-Hoover thermostat.[42,43] It adds an additional degree of freedom into the system's Hamiltonian, and as a result one more equation needs to be integrated along with the usual spatial coordinates and momenta equations. A detailed description of our implementation of this thermostat can be found in Ref.[44]

An extended ensemble that was implemented in this project is the isothermal-isotension ensemble (NtT), where t is an external stress tensor. This ensemble was used for two purposes. One, to test our potential by looking at the system behavior vs. temperature and the second to find the equilibrium shape of the computational box at each temperature for extraction of the HCP lattice parameters a and c. This was achieved by letting the system expand starting from an initial state at T=0 and heating to the chosen temperature T. The correct way to do so is by controlling the system temperature and pressure. By doing so we are allowing all other ther-

modynamical quantities such as the shape, volume and energy of the system to fluctuate. The extended ensemble is a combination of two methods. The first method is the aforementioned Nose-Hoover thermostat. The second method was developed by Parrinello and Rahman[45]. This algorithm allows the size and shape of the system to change by making them dynamical variables, so that phase transitions can be studied in simulations. In our system the external pressure was set to zero, so that our stress tensor t is also equal to zero close to the melting point T_m.

C. Parallel Algorithm

The simulations were performed on a cluster parallel machine[46] which enabled us to achieve system sizes and run times sufficient for our needs. For the bulk simulations, up to 11,664 atoms were used, with periodic boundary conditions in all directions. For the samples having a surface, we simulated up to 32,000 atoms with periodic boundary conditions along two directions and free boundaries along the direction perpendicular to the surface (slab configuration[47]). Because of the non-Bravais structure, implementation of the periodic boundary conditions was somewhat complicated. We found that the run times needed to equilibrate and then average over fluctuations near melting are very long, and so the use of parallel code to speed up the calculations turned out to be essential. The parallel algorithm is a spatial decomposition, using MPI, implemented on NANCO, which is a 128 dual-core processor (2.2 GHz AMD Opteron) LINUX cluster with an infiniband interconnect. The sample sizes are not enormous, indeed in preliminary tests of our parallel code with a Lennard Jones potential tuned to argon we reached one million atoms. However the equilibration and runtimes are much longer here so smaller samples were mainly used, with size scaling tested for selected sizes only. Details of the parallel algorithm and speedup were already given elsewhere for both the argon and magnesium samples.[48].

D. Visualization

With such a complex lattice, visualization of the samples was essential for the debugging phase. We used AViz,[49] an OpenGL/MESA package for atomistic simulation developed at the Technion. The visualizations enabled us to observe at a glance when boundary conditions were correct (otherwise the samples were usually unstable over even short times). Once we were certain the samples were behaving correctly we again used visualization - this time layers of atoms were color coded in accordance with the initial positions in order to determine when layer mixing begins, signalling the onset of melting. Images of initial $T = 0$ and final $T = T_m$ surface melting samples are shown at the left of Figure 2.The image on the right will be described more completely in the results section, but we note that the atoms above and below the initial box indeed indicate increased layer spacing near the surface. Since we are only visualizing one replica of a sample with parallel boundary conditions in the direction perpendicular to the surface, atoms exiting the box at the sides are actually moving to the other side of the periodic boundary condition wall. As will be described in the following sections, once the correct temperature windows were determined, sufficient data were accumulated for order parameters, elastic constants etc., to obtain good statistics.

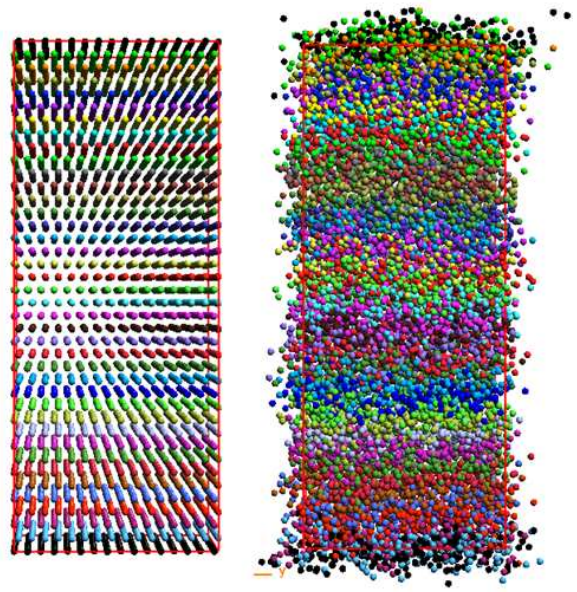

FIG. 2: (color online) Visualization of a slab having 2 free**c** (0001) surfaces at the top and bottom. Atoms in different layers are color coded to allow easy detection of interlayer diffusion. Left panel: initial state at T=0. Right panel: molten state, T=970K. Note how the layers become mixed, especially near the the top and bottom surfaces of the sample.

III. MECHANICAL MELTING

The simulations of melting in the bulk described in this section were intended both to check the implementation of our potential and to investigate the changes of the mechanical properties of the system up to the melting temperature. We did not make extensive finite size scaling tests, but did test different sample sizes to select the optimal one for our study. The validation confirms that that the sample sizes used indeed exhibit the phenomena we are looking for. The bulk samples had periodic boundary conditions in all directions. Because of the non-Bravais nature of the HCP lattice the number of atoms in each direction is twice that along a row of a single plane. For our longest simulation we choose 36 atoms in each direction to give a total of 324 atoms in each xy plane (18×18

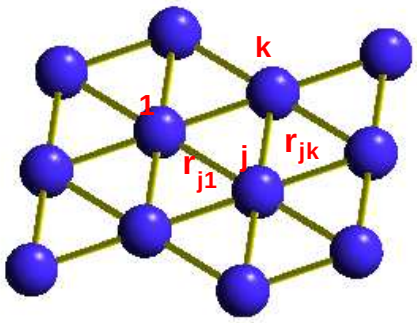

FIG. 3: (color online) A single XY plane of the HCP lattice of the bulk simulation. The atoms are labelled to clarify the definition of the structural order parameter, with atoms explicitly labelled by 1, j and k, and distances r_{j1} and r_{jk} are shown.

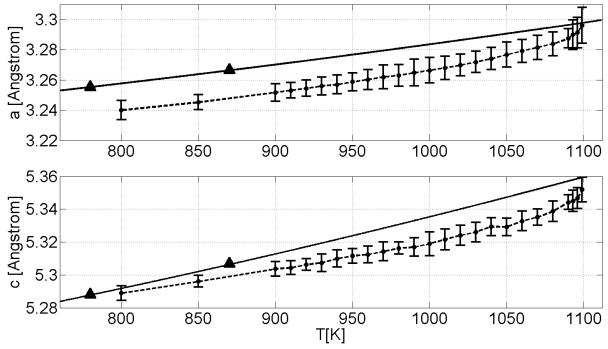

FIG. 4: Temperature dependence of the a and c lattice parameters. Closed circles connected by a dashed line are the result of the simulations, solid line is a linear fit to experimental data (triangles) available in this temperature range[50].

atoms). We chose a total of 36 such layers, giving a total number of atoms of 11664.

Two structural order parameters were used for the bulk calculations. Atoms $j = 1, N$ interact with their six neighbours. Referring to Figure 3, we show an atom explicitly labelled as 1, two of its neighbours, j and k, and the distances r_{j1} and r_{jk}. One order parameter, η_{XT}, describes the crystalline order in the XY plane which is a triangular lattice by measuring the angle between nearest neighbors which should be 60° and is defined through

$$\eta_{XY} = \left\langle \frac{1}{5N} \left| \sum_{j=1}^{N} \sum_{k=2}^{6} \exp\left[i6 \arccos\left(\frac{\vec{r}_{j1} \cdot \vec{r}_{jk}}{a^2} \right) \right] \right| \right\rangle \quad (1)$$

where N is the number of atoms, a is the lattice parameter calculated by averaging over the distance of each of the 6 neighbors of a given atom in the same XY plane. Values of a presented below are averaged over all the atoms in the crystal. The angular brackets denote averaging over time.

The second order parameter, η_Z describes the separation between the triangular layers in the z direction. It is defined through

$$\eta_Z = \left\langle \frac{1}{N} \left| \sum_{j=1}^{N} \exp\left[i \left(\frac{2\pi}{c/2} \hat{z} \cdot \vec{r}_j \right) \right] \right| \right\rangle \quad (2)$$

where c is the lattice constant calculated by averaging over the nearest neighbor distance along the z axis.

Several simulations of some 10^6 steps each were performed to check the stability of the system under the NtT algorithm. The external pressure was set to zero. During the simulation different properties were measured, including the lattice parameters, internal temperature, internal pressure, order parameters, and potential energy. We found that the system stabilized after about 50,000 time steps. The simulations succeeded in estimating values of the lattice parameters as a function of

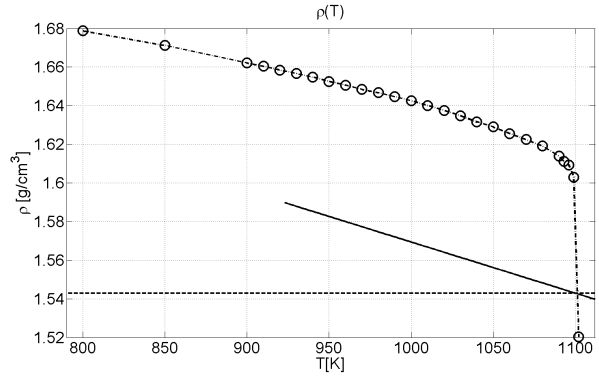

FIG. 5: Temperature dependence of the density of solid Mg. Open circles connected by the dashed line are the results of our simulation. The solid line is extrapolated from experimental values of the density of the liquid in this temperature range[51] and the horizontal dashed line is the liquid density at $1100K$.

temperature with good accuracy, deviations from the experimental values[50] being less then 0.5% .

The results of the thermal expansion of the a and c lattice parameters are shown in Fig. 4. The statistical errors in the values of the lattice parameters are less than 0.5% of the average value. The simulated result are in excellent agreement with the extrapolated experimental data[50] up to the bulk melting temperature, which was determined to be $T_b = 1102 \pm 3K$. The ratio between T_b and the experimental melting temperature of 923K is very close to 1.2, a ratio found also in other systems[52]. The next important result is the decrease of the density due to thermal expansion, with results shown in Fig. 5. The linear decrease of the density with temperature terminates at T_b. At this temperature, the volume of the sample jumps by more than 1% ,consistent with a first order phase transition from solid to liquid. As shown in the figure, the density of the liquid at T_b is in good agreement with the experimental value[51]. We conclude that

both the potential and the simulation algorithm give a satisfactory description of the bulk phase of Mg.

IV. THERMODYNAMIC MELTING

We next investigated surface disordering and premelting as a function of temperature up to the thermodynamical melting temperature T_m. Results include the thermodynamic melting point of our model, and the variation of the structural and energetic properties as a function of temperature. We investigated samples with three surface orientations: **c** (0001) , **a** ($10\bar{1}0$) and **s** ($10\bar{1}1$)) . The location of these facets on the equilibrium crystal shape at T=0 was shown in Fig.1.

To describe sample geometries for the three facets, we reassign the the axiz labels x, y and z as appropriate for each case, and begin with a general description. Our initial configuration is an infinite slab (in the x and y directions) with two initially identical free surfaces, normal to the $+z$ and $-z$ directions. We made simulations using slabs containing a total of 40, 60 or 80 layers. The atoms in each plane were arranged in arrays of 8x8, 16x16 or 20x20. Most of the calculations were made using samples of 40 layers with 16x16 atoms in each plane. There are no "frozen" layers in our samples, unlike in Sorkin et al.[19] because the samples are much larger and so the two surfaces melt while the center remains solid.

For each orientation of the slab, the axes were rotated so that the normal to the surface is always in the z direction. Periodic boundary conditions were applied in the xy plane. Table I summarizes the distances between nearest-neighbor atoms in the x, y and z directions (after rotation) and the in-plane surface density, ρ_s, in units of the two lattice constants a and c. There are two aspects of the geometry which are due to the nature of a non-Bravais lattice. The first remark applies to the **s** facet, ($10\bar{1}1$), where there are two atomic planes very close to each other, separated by ~ 0.4Å. This distance is much smaller than the cutoff distance of our potential (7.5 Å), nearest neighbour separation(3.9 Å), and the distance to the next layer(≈2.4 Å). In this case, we expect that the dynamics of these two close layers will be strongly correlated, so there is no point in discussing them separately. Hence, we display our results with these two adjacent planes treated as a single layer. The second aspect is relevant to all facets: there is no reflection symmetry in the xy plane; it exists only for the z direction. This was taken into consideration mainly in the measurements of the order parameters for each axis. The arrangement of the atoms in each of the planes is shown in Fig. 6. On substituting the values of the lattice constants for the **a** and **c** directions, one finds that the in-plane density ρ_s satisfies $\rho_s(0001) > \rho(10\bar{1}1) > \rho(10\bar{1}0)$. Here, we consider the two nearby planes of an **s** facet as one. This choice will become important later on.

In the first part of each simulation (5×10^4 steps) the system reached internal equilibrium. In the second part, measurements were made over 9.5×10^5 steps. Extending the simulation further did not improve the statistics significantly. Simulations with different number of layers and/or atoms in a single layer were also performed. In the xy plane we varied the number of atoms between 8×8 up to 20×20. Too small an array emphasized the periodic boundary conditions, due to the large cutoff radius of the potential (7.5 Å). Along the z axis we made simulations with 40, 60 and 80 layers. We found that additional layers beyond 40 had no significant qualitative influence on the final results and discuss this further in the next subsection.

Surface	a_x	a_y	a_z	ρ_s
Mg(0001)	$a/2$	$\sqrt{3}a/2$	$c/2$	$2/(\sqrt{3}a^2)$
Mg($10\bar{1}0$)	$\sqrt{3}a/2$	$c/2$	$a/2$	$2/(\sqrt{3}ac)$
Mg($10\bar{1}1$)	$a/2$	$\sqrt{a^2+c^2}/2$	$\frac{ac\sqrt{3}}{\sqrt{4c^2+3a^2}}$	$\frac{1}{a\sqrt{a^2+c^2}}$

TABLE I: List of nearest-neighbor atom distances along x, y and z, and of surface density for all 3 facet orientations

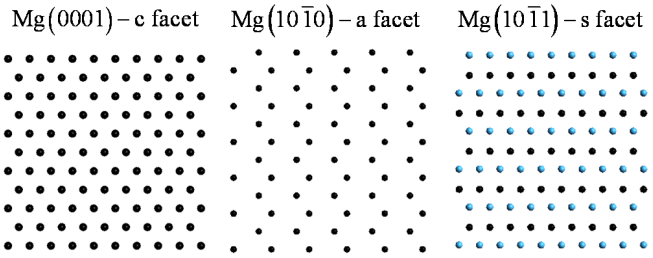

FIG. 6: (color online) Spatial distribution of atoms within a layer for all the facets. The size of each facet is 30×30 Å^2.

A. Structural order parameters

For each surface orientation, the order parameters measure the degree of spatial correlations of the atoms in each layer. They take the same functional form as those of the bulk, but instead of being averaged over the entire sample, are now summed over specific layers, and instead of merely considering one parameter in the xy plane and another in the z direction, we now consider all three directions. In a perfect initial state all order parameters are unity, except for one which will be discussed below. As the temperature increases the value of the order parameter decreases. We define the order parameter of the

lth layer by:

$$\eta_{l,\alpha} = \left\langle \frac{1}{n_l^2} \left| \sum_{j \in l} \exp\left(i \vec{g}_\alpha \vec{r}_j\right) \right|^2 \right\rangle \quad (3)$$

where α denotes the coordinate x,y, or z and the vector $\vec{g}_\alpha$ stands for $\frac{2\pi}{a_\alpha}\hat{\alpha}$. This set of vectors defines a set of different axes, with a_α being the nearest-neighbor distance in the α direction (From Table I) and n_l the instantaneous number of atoms in the layer l. The sum extends over the particles in layer l and the angular brackets denote averaging over time. Equation 3 describes all the order parameters except that for the (0001) surface where each layer forms a triangular lattice. In this case both order parameters for the x and y directions measure the angle between nearest neighbors, which is 60° in the ordered state. Its definition is:

$$\eta_{l,xy} = \left\langle \frac{1}{n_l^2} \left| \sum_{i \in l} \sum_{j=2}^{6} \exp\left[i6 \arccos\left(\frac{\vec{r}_{i1} \cdot \vec{r}_{ij}}{a^2} \right) \right] \right|^2 \right\rangle \quad (4)$$

Finally, the order parameter for the z direction of the sample with the **s** facet has an initial value of 0.75 instead of 1, because here we combine two layers with separation of about 0.4 Å and the center of mass of these planes is in the middle. Figure 7 show the temperature dependence of the order parameters of the surface layer on all 3 facets. We chose to show the results for the second layer, since the topmost layer is additionally disordered due to promotion of atoms into the adsorbed layer (adlayer). The order parameter decreases markedly with temperature as a result of thermal vibrations and defect formation, effects which are more pronounced on the surface. It is seen that the order parameter on the **a** facet is negligibly small already at 900K ($\sim 10^{-2}$), reaching a limiting value around 930K (Fig.7). A similar situation takes place on the **s** facet, while on the **c** facet the order parameter is larger and remains so to higher temperatures. This indicates that in our simulation, melting begins at the **a** facet and that the second layer is in the liquid state at 930K. In the real system, all the facets share edges (Figure 1) and so the molten phase would be able to propagate from one facet onto another in this way. In the simulations however, the periodic boundary conditions in the xy plane effectively suppress the propagation of the liquid phase onto the other facets, allowing the **c** facet to superheat. The very onset of disorder, which starts on the **a** facet, is however independent of this decoupling and retains its quantitative significance. The difference between the simulated melting temperature and the experimental melting temperature $923K$ can caused by several processes. Our production samples have only 40 layers because a systematic study with larger sample sizes would have required impractical total runtimes. Tests with samples of 60 and 80 layers in the z direction for the a facet found a few degree higher higher temperature for the larger samples.[44]

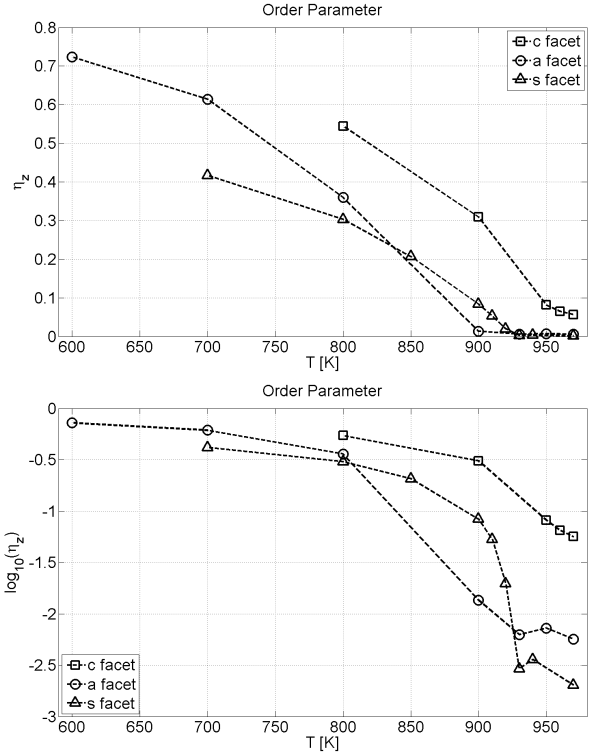

FIG. 7: Structural order parameter of the topmost second layer for all 3 facets as a function of temperature. Upper panel - linear scale and lower panel - logarithmic scale.

B. Local density profile

A local density profile $\rho(z)$ is defined as the average number of atoms in a slice of width Δz where z is the direction normal to the surface. Following Chen et al.[16,17], $\rho(z)$ can be represented by a continuous function defined as

$$\rho\left(z\right) = \left\langle \frac{1}{\sqrt{2\pi\Delta z^2}} \sum_i \exp\left(-\frac{\left(z - z_i\right)^2}{2\Delta z^2} \right) \right\rangle \quad (5)$$

where z_i is the z coordinate of i-th atom , with $z = 0$ set at the bottom of the slab. The angular brackets indicate time average. For each direction, Δz was set as 0.1 of the mean distance between layers in that particular sample. One feature which can be seen using local density profiles is premelting. This process can be examined by monitoring the layer by layer modulation of the density profile of the system at various temperatures. Figures 8- 10 show results for **c**, **a** and **s** facets, respectively. One sees that at low temperatures the density profile $\rho(z)$ consists of a series of sharp, well resolved peaks. As the temperature increases, the effective width of each layer becomes broader due to the enhanced atomic vibration and the position of the peaks move to larger values of z due to the thermal expansion. At temperatures close to T_M the atomic vibrations become so large, especially in the surface layers, that disorder sets in, with atomic migration

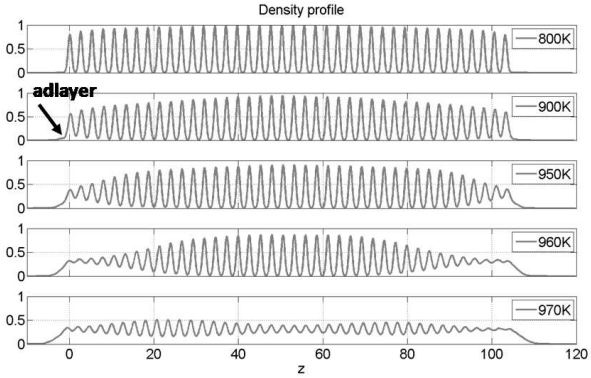

FIG. 8: Density profile across (0001) along the z direction perpendicular to the surface at various temperatures, as indicated. The density is normalized relatively to the maximum density at low temperature.

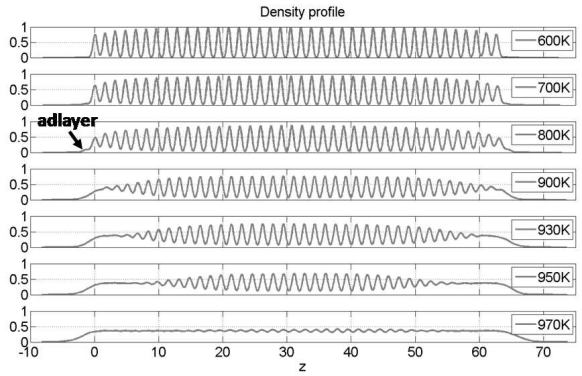

FIG. 9: Density profile across $(10\bar{1}0)$ along the z direction (normal to the surface) at various temperatures, as indicated. The density is normalized relatively to the maximum density at low temperature.

taking place between the layers. Evidence for this is given by the fact that the minima of $\rho(z)$ between two peaks rise to non-zero values. This is a reminiscent of a liquid-like structure, suggesting that the system is crossing over to a state of 'premelting'. In parallel, the density of the topmost layer becomes slightly lower. The loss of density is accompanied by the appearance of adatoms on top of the first surface layer, forming an adlayer. The generation of adatom-vacancy pairs induces disorder and eventually the topmost layers become a thin quasiliquid film. The 'premelting' phase begins on each facet at a different temperature, $\simeq 700K$ for $(10\bar{1}0)$ and $\simeq 850K$ for $(10\bar{1}1)$, and $\simeq 900K$ for (0001). We note that premelting appears first at the $(10\bar{1}0)$ surface, which is the least dense. These results support our understanding that melting starts on the **a** facet. The other surfaces show disorder, but do not melt, being "protected" by the absence of contact with the **a** facet. Regarding the adlayer, it first appears on the least packed surface $(10\bar{1}0)$, then on at $(10\bar{1}1)$ surface and finally on the close packed surface (0001). As we show below, most of the adatoms in the adlayer come from the top 2-3 layers. This hierarchy is in agreement with other simulations which investigated surface premelting of FCC and BCC metals such as Al[16], Ni[17] and V[19]. In all these case, as the temperature increases, the adlayer appears first on the least packed surface and last on the closest packed surface.

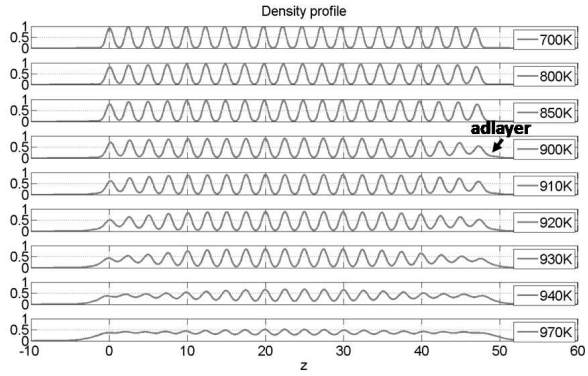

FIG. 10: Density profile across $(10\bar{1}1)$ along the z direction (normal to the surface) at various temperatures, as indicated. The density is normalized relatively to the maximum density at low temperature.

C. Distance between layers

Structural information, such as an interlayer relaxation and thermal expansion at the surface can be calculated directly from the difference between the average distances between the ith and $(i+1)$ layers:

$$d_{i,i+1} = \left\langle \frac{1}{n_{i+1}} \sum_{j \in i+1} z_j - \frac{1}{n_i} \sum_{j \in i} z_j \right\rangle \qquad (6)$$

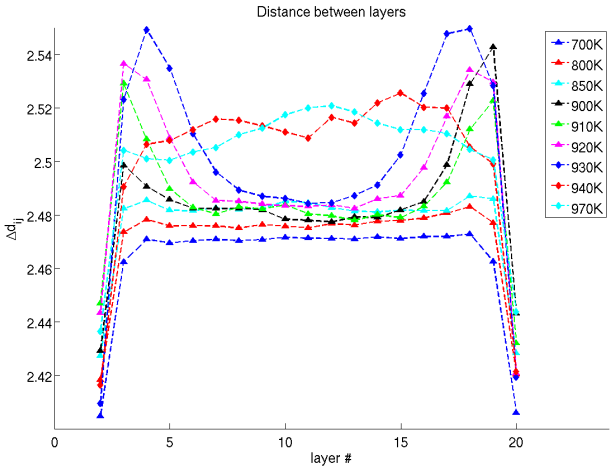

FIG. 11: (color online) Profiles of the distance between neighboring layers across the slab with a $(10\bar{1}1)$ surface orientation at selected temperatures.

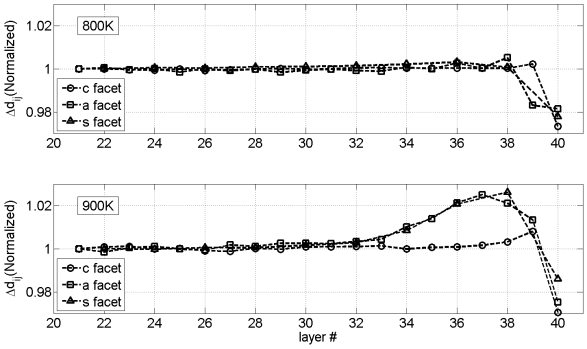

FIG. 12: Interlayer distances, normalized by the center layer distance ("bulk" distance) of c, a and s at 800K and 900K. Layer ♯20 is in the center of the slab, while layer ♯40 is the surface layer.

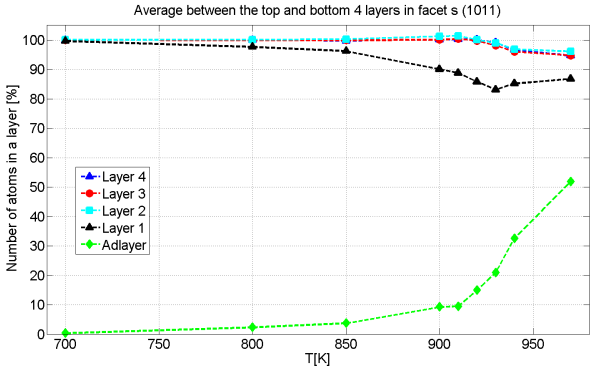

FIG. 13: Layer occupation of the $(10\bar{1}1)$ sample as a function of temperature.

where z_j is the z coordinate of the j-th atom , the sum includes atoms in the layers i and $i+1$ and the angular brackets denote averaging over time.

The top surface layer exhibits an inward relaxation for all the facets. This can be observed in Fig. 11 of the **s** facet. This well known inward relaxation is a consequence of the lower electron density at the surface, relative to the bulk. The sample compensates for this 'deficit' by contracting the distance between the first and second layers. The next several layers exhibit a outward relaxation which becomes more prominent with increasing temperature. We illustrate this effect in Fig. 12 which shows the normalized values of $d_{i,i+1}$ of all the layers at 800K and 900K for all 3 facets. It is noticeable that the **c** is most stable, having the lowest interlayer relaxation. In general, the thermal expansion of the surface layers is larger than the thermal expansion of the layers in the center of the sample. The difference in the geometry of the various samples is reflected in the thermal expansion of their surface region, where a surface which is less packed expands more than a close packed one. This is especially evident in the results at 900K in Fig. 12

Finally, we use these data to pinpoint the melting temperature T_m. Looking at Fig. 11 for the **s** facet one can clearly see a large positive change of $d_{i,i+1}$ which takes place between 920K and 930K, indicative of a volume change. Furthermore, this increase is accompanied by a transition to a state where $d_{i,i+1}$ is very uniform across the sample, something expected from a liquid. An uniform molten state across the whole sample can be observed since we do not use any "frozen" layers. Similar behaviour is seen with the other facets. We found that the vibration amplitude of the atoms at the surface[44] reaches a saturated value above 930K, which again indicates a transition to the liquid state. From these data we conclude that the melting transition in our model system takes place between 920K and 930K, close to the experimental value of 922K.

D. Layer occupation and energetics

The occupation of the layers close to the surface changes with temperature due to the creation of adatom-vacancy pairs and interlayer diffusion. The inner layers keep most of their atoms at all temperatures. Here, we focus on the occupation of the 4 outmost layers, and of the adlayer. Figure 13 show the occupation of each of the outermost 4 layers and of the adlayer. The values in these figures are an average of the two free surfaces in our sample, at the top and at the bottom in each slab. The formation of an adlayer begins first on the least packed surface $(10\bar{1}0)$ at around $T = 600K$, then at the s facet $(10\bar{1}1)$ at about $T = 700K$ and finally at the close packed surface c (0001) at around $T = 800K$.

The creation of an adlayer initially involves the generation of vacancies in the first surface layer. At higher temperatures, depending on the facet, vacancies begin to appear in the underlying layers (second, third and fourth) due to promotion of atoms to vacant positions in the first surface layer via the vacancy migration mechanism. Atom migration from the deeper layers increases significantly as the temperature approaches the melting point, see Figure 2. The number of vacancy-adatom pairs is larger on the least packed surface $(10\bar{1}0)$ than on the other surfaces. The correlation between number of atoms in the first layer and the adlayer is obvious from Fig. 13, suggesting that practically all adatoms come from the first surface layer.

The same effect, that of disordering and gradual thickening of the surface region was observed in computer simulation of surface premelting for FCC and BCC metals[16,17,19,24,25]. In all the simulations, including ours, the least packed surfaces, (110) in FCC, (111) in BCC and $(10\bar{1}0)$ in HCP begin to disorder first, while the most closely packed surface (111) in FCC, (011) in BCC and (0001) in HCP preserve their ordered crystalline structure almost up to the melting point. Even so, near T_m, the number of atoms in the adlayer on all surfaces is well over 1% of the total number of atoms per layer.

Once in thermal equilibriun, we can count the average

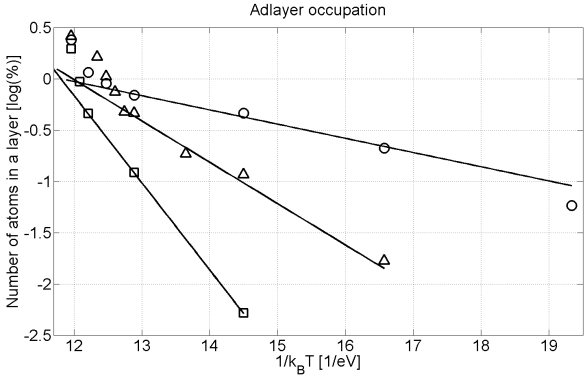

FIG. 14: Adlayer occupation of all facets as a function of inverse temperature (Circles - a facet, triangles - s facet, squares - c facet). The lines are exponential fits to data in the temperature region where the adlayer occupation is less than 1% of a complete layer.

number of atoms in the adlayer. The adlayer occupation as a function of temperature allows us to estimate the formation energy E_s of an adatom-vacancy pair according to the relation:

$$n \equiv \frac{N_{Adlayer}}{N_{Atoms}} \propto \exp\left(\frac{-E_s}{k_B T}\right) \tag{7}$$

where n is the adlayer occupation. Eq. 7 is valid for small adlayer occupation (less than 1% of the atoms in a layer) and so the temperature range used for the fit was accordingly restricted. The fits of the adlayer occupation vs. temperature to the Boltzmann factor $\exp(-E_s/k_BT)$ are shown in Figs. 14 for the (0001), $(10\bar{1}0)$ and $(10\bar{1}1)$ facets. The results of the fit for E_s are summarized in Table II. Data from other elements with different lattice structure such as vanadium (BCC) and copper (FCC)[53] also show that the close packed facet has the largest formation energy while the least packed facet has the lowest.

Surface	(0001)	$(10\bar{1}0)$	$(10\bar{1}1)$
Mg HCP E_s	$1.95 \pm 0.20eV$	$0.31 \pm 0.04eV$	$0.92 \pm 0.10eV$

TABLE II: Energy of surface defects (adatom-vacancy pairs) calculated using the adlayer occupation data of the various surfaces.

It is physically expected that the facet which becomes disordered first will have the lowest formation energy E_s, and indeed the low density **a** facet follows this rule. At the other end the close packed **c** facet has the largest formation energy. This was also observed in the cubic systems referenced earlier.

V. SUMMARY

In conclusion, in this study we have simulated the temperature dependence of several properties of HCP Mg, such as lattice parameters in the bulk and on surfaces, and surface disorder arising via formation of structural defects. Our results confirm that the hierarchy where premelting phenomena first appear on the least dense surface also holds for an HCP metal. Melting indeed begins at the $(10\bar{1}0)$ surface Mg which is the least dense.

A comphrehensive set of results and figures similar to those presented above for additional facets and more temperatures can be found in Ref.[44]. Color animations of the melting processes can be found at the website[54].

Acknowledgments This work was supported by Israel Science Foundation and by the Technion Fund for Research. We thank the Russel Berrie Nanotechnology Institute for computer time on the NANCO computer.

* Electronic address: phr76ja@tx.technion.ac.il

[1] A. R. Ubbeldone, Melting and Crystal Structure, Clarendon press, (Oxford) (1965).
[2] F. Lindemann, Z.Phys. **11**, 609 (1910)
[3] Y. Ida, Phys. Rev., **187**, 951, (1969)
[4] M. Born, Journ. of Chem. Phys., **7**, 591 (1939)
[5] J. L.Tallon, Phyl. Mag.A, 39, 151, (1978)
[6] D. Wolf, P. R. Okamoto, S. Yip, J. F. Lutsko and M. Kluge, J. Mater.Res.**5**, 286 (1990)
[7] A. V. Granato, Phys. Rev. Lett. **68**, 974 (1992)
[8] T. A. Weber and F. H. Stillinger, J. Chem. Phys. **81**, 5095 (1984)
[9] R. W. Cahn, Nature **323**, 668 (1986)
[10] R. W. Cahn, Nature **413**, 582 (2001)
[11] A. Kanigel, J. Adler, and E. Polturak, Int. J. Mod. Phys. **C 12**, 727 (2001)
[12] J. W. M. Frenken and J. F. van der Veen, Phys. Rev. Lett. 54, 134 (1985)
[13] J. F. van der Veen, in Phase Transitions in Surface Films 2, edited by H. Taub. et al. (Plenum, New York, 1991)
[14] A. Trayanov and E. Tossati, Phys. Rev. **B 38**, 6961 (1988)
[15] R.N. Barnett and U. Landman, Phys. Rev. **B 44**, 3226 (1991)
[16] E. T. Chen, R. N. Barnett, and U. Landman, Phys. Rev B **41**, 439 (1990)
[17] E. T. Chen, R. N. Barnett and U. Landman, Phys. Rev B **40**, 924 (1989)
[18] V. Sorkin, E. Polturak and Joan Adler, Phys. Rev. B **68**, 174102 (2003)
[19] V. Sorkin, E. Polturak and Joan Adler, Phys. Rev. B **68**, 174103 (2003)
[20] R. Lipowsky, Phys. Rev. Lett. **49**, 1575 (1982)
[21] R. Lipowsky, U. Breuer, K. C. Prince and H. P. Bonzel, Phys. Rev. Lett. **62**, 913 (1989)
[22] O. Tomagnini, F. Ercolessi, S. Iarlori, F. D. Di Tolla and E. Tosatti, Phys. Rev. Lett., **76**, 1118 (1996)

[23] R. Ohnesorge, H.Lwen and H. Wagner, Phys. Rev.E,**50**, 4801, (1994)
[24] H. Hakkinen and M. Manninen, Phys. Rev. B **46**, 1725 (1992)
[25] H. Hakkinen and U. Landman, Phys. Rev. Lett. **71**, 1023 (1993)
[26] Y. Beaudet, L.J. Lewis and M. Persson, Phys. Rev. B **50**, 12084 (1994)
[27] H. Cox, R. L. Johnston and J. N. Murrel, Surf. Sci. **67**, 373 (1996)
[28] P. Stoltze, J. Chem. Phys. **92**, 6306 (1990)
[29] P. Stoltze, J. K. Norskov and U. Landman, Phys. Rev. Lett. **61**, 440 (1988)
[30] J. Q. Broughton, G. H. Gilmer and K. A. Jackson, Phys. Rev. Lett. **49**, 1496 (1982)
[31] J. Q. Broughton and G. H. Gilmer, J. Chem. Phys. **79**, 5119, (1983)
[32] J. Wang, J. Li, S. Yip, S. Phillpot, and D. Wolf, Phys. Rev.**B 52**, 12 627 (1995)
[33] J. Wang, J. Li, S. Yip, S. Phillpot, and D. Wolf, Physica A **240**, 396 (1997)
[34] Z.H. Jin, P. Gumbsch, K. Lu, and E. Ma, Phys. Rev. Lett. **87**, 055703 (2001)
[35] A. Hashibon, J. Adler, G. Baum and S. G. Lipson, Physical Review B 58, 4120, (1998)
[36] D. C. Rapaport, *The Art of Molecular Dynamics Simulation Second Edition*, Cambridge Univeristy Press, (2004)
[37] H. Haile, *MD simulation elementary methods*, Willey, (1989)
[38] D. Y. Sun, M. I. Mendelev, C. A. Becker, K. Kudin, Tomorr Haxhimali, M. Asta, J. J. Hoyt, A. Karma and D. J. Srolovitz, Phys. Rev. B, **73**, 024116, (2006)
[39] Y. Liu, J. B. Adams, F. Ercolessi, and J. A. Moriarty, Modell. Simul. Mater. Sci. Eng. **4**, 293, (1996)
[40] Z. G. Xia, D. Y. Sun, M. Asta and J. J. Hoyt, Phys. Rev. B, **75**, 012103, (2007)
[41] G. Sutmann, Classical Molecular Dynamics, http://www.fz-juelich.de/nic-series/volume10
[42] S. Nose, Molec. Phys., **81**, 511, (1984)
[43] W. G. Hoover, Phys. Rev. A, **31**, 1695, (1985)
[44] Pavel Bavli, M.Sc. thesis, Technion, (2009)
[45] M. Parinello and A. Rahman, Phys. Rev. Lett., **45**, 1196, (1980)
[46] http://phycomp.technion.ac.il/ nanco
[47] S. R. Phillpot, S. Yip, and D. Wolf, Computers in Physics **3**, 20 (1989)
[48] P. Bavli and Joan Adler, Physics Procedia, **4**, 3-7, (2010)
[49] J. Adler, Computers in Science and Engineering, **5**, 61-65, (2003)
[50] H. E. Friedrich and B. L. Mordike,*Magnesium Technology*, Springer (2006)
[51] http://www.magnesium.com/w3/data-bank/index.php?mgw=153
[52] K. Lu and Y. Li, Phys. Rev. Lett. **80**, 4474 (1998)
[53] S. Sorkin, Ph.D thesis, Technion (2006)
[54] http://phycomp.technion.ac.il/∼ phr76ja/pavelpage.html